nature COMMUNICATIONS

ARTICLE

Received 19 Apr 2011 | Accepted 21 Sep 2011 | Published 18 Oct 2011

DOI: 10.1038/ncomms1514

Field-effect reconfigurable nanofluidic ionic diodes

Weihua Guan[1], Rong Fan[2] & Mark A. Reed[1,3]

Several types of nanofluidic devices based on nanopores and nanochannels have been reported to yield ionic current rectification, with the aim to control the delivery of chemical species in integrated systems. However, the rectifying properties obtained by existing approaches cannot be altered once the devices are made. It would be desirable to have the ability to modulate the predefined properties *in situ* without introducing external chemical stimuli. Here we report a field-effect reconfigurable nanofluidic diode, with a single asymmetrically placed gate or dual split-gate on top of the nanochannel. The forward/reverse directions of the diode as well as the degrees of rectification can be regulated by the application of gate voltages. Compared with the stimuli-responsive tuning of the rectification properties, the electrostatic modulation offers a fully independent and digitally programmable approach for controlling the preferential conduction of ions and molecules in fluids. This device would serve as a building block for large-scale integration of reconfigurable ionic circuits.

[1] Department of Electrical Engineering, Yale University, New Haven, Connecticut 06520, USA. [2] Department of Biomedical Engineering, Yale University, New Haven, Connecticut 06520, USA. [3] Department of Applied Physics, Yale University, New Haven, Connecticut 06520, USA. Correspondence and requests for materials should be addressed to M.A.R. (email: mark.reed@yale.edu).

With applications ranging from biosensing to the control of molecular transport, synthetic nanopores and nanochannels are the focus of growing scientific interest[1]. Analogous to a solid-state semiconductor diode for regulating the flow of electrons/holes to one preferential direction, nanofluidic diodes are being developed to achieve the rectified ionic transport-ions favourably move in one direction and are inhibited in the opposite direction. Such rectification effect is of great importance owing to its relevance to biological ion channels[2]. Moreover, ionic diodes, together with ionic transistors[3–9] represent the key building blocks for ionic circuits[10,11], which would allow for regulating[6], sensing[12], concentrating[13] and separating[14] ions and molecules in electrolyte solutions, mimicking voltage-gated ion channels in a variety of biological systems.

Several nanofluidic platforms based on nanopores and nanochannels were reported to produce ionic current rectification by symmetry breaking[15] in geometries[16–19], surface charge distributions (either intrinsic material properties[20,21] or chemically modified properties[22,23]), bath concentrations[24], or a combination of them, for example, by positively and negatively patterning charged regions in conical nanopores[25]. Nevertheless, it has not been possible to change the predefined rectifying properties obtained by these approaches once the devices are made. Although several externally tunable methods have been proposed so far, most of them aim to alter the nanochannel wall property by introducing external chemical stimuli, for example, hydronium ions (pH)[26–28], enzymes[29] and polyvalent cations[30]. All these methods require changing the native environment of the solution being transported. Contrary to the chemical stimuli-responsive schemes, an electric field normal to the nanochannel walls is able to enhance or diminish the ionic concentrations near the surface *in situ*[3–9], resembling the carrier number modulation in a metal-oxide-semiconductor field-effect transistor.

Here we report a field-effect reconfigurable ionic diode by asymmetrically modulating the cation/anion ratios along the nanochannel. The field-effect approach requires no solution replacement and allows large-scale integration for more complex functions. A key feature of our device is that it allows the post-fabrication reconfiguration of the diode functions, such as the forward/reverse directions as well as the rectification degrees. These results may lead to the creation of reconfigurable ionic circuits, an ionic counterpart of the electronic field-programmable gate array.

Results

Device structure. The schematic structure of the nanofluidic field-effect reconfigurable diodes (FERD), and the experimental setup is illustrated in Figure 1. The FERD is a three-terminal device that has a similar structure to a nanofluidic field-effect transistor (FET)[6,7], yet with a critical difference that the gate electrode of FERD is asymmetrically located near one of the microfluidic reservoirs. The control devices with gate electrodes sitting symmetrically along the nanochannel were also fabricated on the same silicon wafer. We used a sacrificial layer method to produce the nanochannels (20 nm in height) with a novel 'bond-followed-by-etch' scheme, which completely avoids the nanochannel collapse problem encountered in conventional 'etch-and-bond' schemes (Supplementary Fig. S1 and Supplementary Methods). To make a consistent notion in the following discussion, we denote the microfluidic reservoir that is close to the gate electrode as *Cis* (C) and the other reservoir far away from the gate electrode as *Trans* (T).

Nanochannel characterization. We first carried out experiments on the electrical characterization (Supplementary Fig. S2) of the nanochannels with the gate terminal floating. By measuring the nanochannel conductance as a function of KCl concentration (C_b), we observed a linear dependence of channel conductance on C_b in the high-concentration regime and a conductance plateau in the low-concentration regime (Fig. 2). The transition concentration is around 1 mM, at which the corresponding Debye screening length (λ_D) is around 10 nm, equal to half of the designed nanochannel height. This behaviour confirms a surface-charge governed ionic

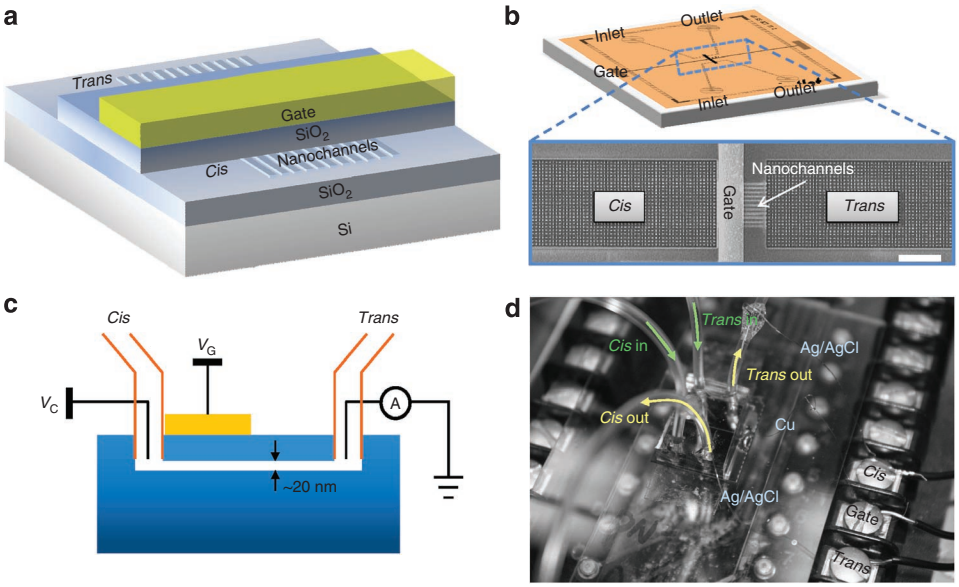

Figure 1 | Device structure and experimental setup. (**a**) Schematic of the nanofluidic FERD. (**b**) Sketch of the planar layout for the assembled device. Two microfluidic channels deliver the electrolyte solutions to the *Cis* and *Trans* reservoirs, formed by SiO_2 trenches with supporting pillars, as shown in the magnified scanning electron microscope (SEM) image. The scale bar in the SEM image is 100 μm. There are 11 parallel nanochannels connecting *Cis* and *Trans* reservoirs. The supporting pillars prevent the microfluidic polydimethylsiloxane from collapsing into the reservoirs. (**c**) Schematic of the electrical and fluidic connection configurations. The electrical contacts are made of Ag/AgCl electrodes and are integrated with the connecting tubes, serving as a low resistive loss contact. V_G and V_C denotes the voltage on the gate and *Cis*, respectively. The *Trans* side is referenced as ground in all measurements in this study. The whole setup is placed in a Faraday cage to shield the electrostatic noise. (**d**) Photograph of a FERD device with electrical and fluidic connections.

transport property[31,32]. By knowing the dimensions of the lithographically defined channels, the surface charge density (σ_s) can be derived by fitting the experimental data (Supplementary Methods). We tested two individual devices fabricated on the same wafer but with different channel width W (2 μm×11 and 3 μm×11, respectively). Both of them can be well fitted by a same σ_s (-2 mC m^{-2}), suggesting the surface properties remain consistent and reliable after the 'bond-followed-by-etch' process. This σ_s value is close to those reported with the plasma-enhanced chemical vapour deposition SiO_2 (~-4.5 mC m^{-2})[20,24].

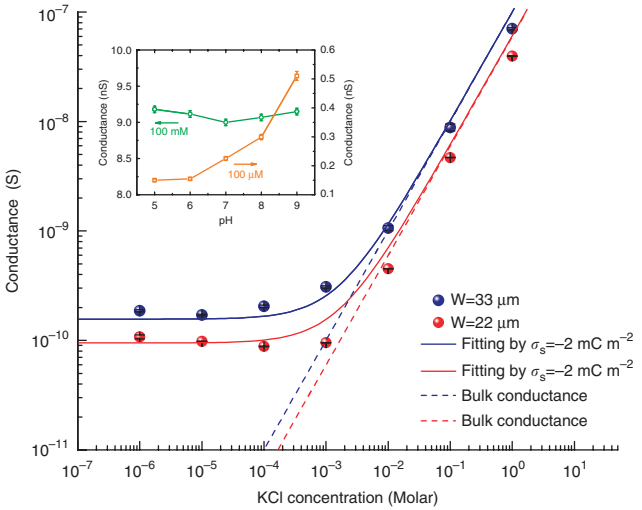

Figure 2 | Measured conductance as a function of KCl concentrations for two devices. Both devices were fabricated using the identical process on a same wafer with gate terminal floating (Blue: $W=33$ μm, $L=100$ μm, $H=20$ nm. Red: $W=22$ μm, $L=100$ μm, $H=20$ nm). Solid lines are the fitting curves with $\sigma_s=-2$ mC m^{-2}. Dashed lines are the bulk prediction that deviates from the experimental data in the low ionic concentration region. The error bars correspond to ten measurements and are smaller than the size of the symbol used. Inset shows the pH dependence of channel conductance at two electrolyte concentrations ([KCl] = 100 μM and [KCl] = 100 mM). The pH of the electrolyte solution is adjusted by adding hydrochloric acid or potassium hydroxide into 100-μM phosphate buffers. The error bars correspond to ten measurements.

AS the surface charge can be modified by changing the solution pH, we further tested the pH dependence of the nanochannel conductance at fixed KCl concentrations (inset of Fig. 2). At high KCl concentrations (100 mM), changing the pH value has negligible impact on the channel conductance, whereas at low KCl concentrations (100 μM), pH has a pronounced impact. This behaviour can be well explained by surface charge governed transport property. At high ionic concentrations, the double layer conductance (which is regulated by pH values) is overwhelmed by the bulk conductance. Therefore, the channel conductance will not change by varying pH. At low KCl concentrations, the channel conductance is dominated by the double layer and is thus pH-dependent. As [H^+] for a given electrolyte concentration decreases, the number of SiO surface charges increases[33].

Field-effect reconfigurability. After verifying that the device conductance is indeed governed by the ion transport in the nanochannels (instead of leakage paths), we went on to investigate the field-effect tunability of the three-terminal FERD devices using electrical configurations shown in Figure 3a. The channel current as a function of *Cis* to *Trans* voltage (V_{CT}) was measured under various gate voltages (V_G). Figure 3b shows the representative current-voltage (I–V) curves obtained with V_G of different polarities, using a 100-μM KCl solution. A clear gate-voltage controlled rectifying property is observed. At $V_G=0$ (middle panel, Fig. 3b), the I-V curve is symmetric with respect to the origin. At a negative gate voltage (left panel, Fig. 3b), the ionic current in the positive V_{CT} regime is higher than that in the negative V_{CT} regime. While at a positive gate voltage (right panel, Fig. 3b), the negative V_{CT} conducts more ionic current than the positive V_{CT}. Consequently, it is possible to switch the preferential direction of the ionic flow via adjusting the external gate voltage, a novel mechanism of nanofluidic control that has never been shown before.

We note that an electric potential barrier will develop at the micro/nano channel interface[34], which is analogous to a potential barrier at a heterojunction in semiconductor devices due to a work

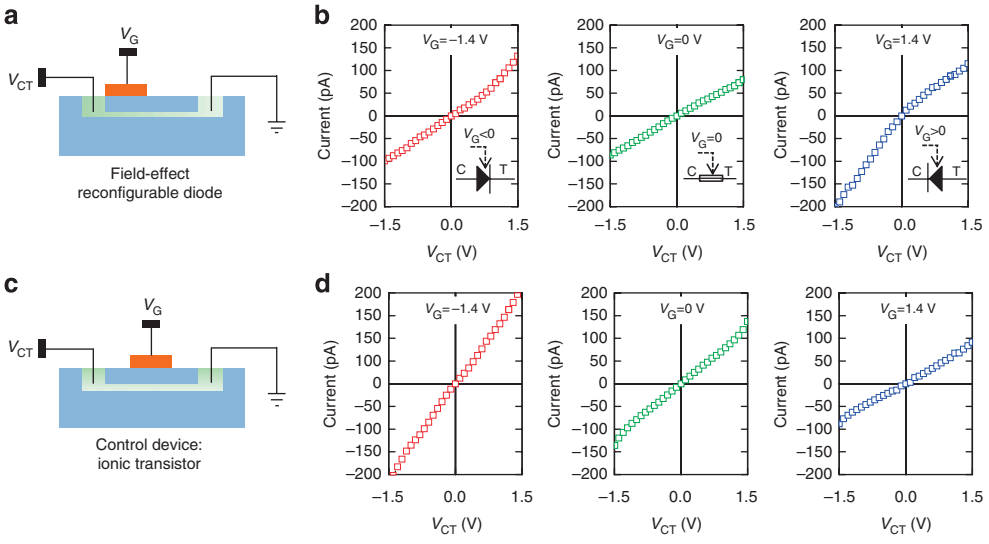

Figure 3 | Current-voltage (I-V) curves for the FERD devices with different gate voltage (V_G) polarities. (**a**) Testing configurations for the FERD device. (**b**) I-V curves for FERD devices ($W=2$ μm×11, $L=100$ μm, $H=20$ nm) using a 100-μM KCl solution. An apparent gate voltage-controlled rectifying property is observed. The inset symbols schematically show the forward direction switched on positive and negative gate voltages. (**c**) Testing configurations for the control transistor device. (**d**) I-V curves for the control device ($W=3$ μm×11, $L=100$ μm, $H=20$ nm) using a 100-μM KCl solution. Gate voltage can modulate the channel conductance but no rectifying property is observed.

function difference[35]. This interfacial barrier is indeed a negligible effect in our FERD devices and is not responsible for the voltage tunable rectifying property (Supplementary Fig. S3). This conclusion is further verified by the I–V characteristics of the control devices (with symmetrically placed gate electrodes), schematically shown in Figure 3c. The major structural difference between the FERD devices and the control devices is the location of the gate terminal. No rectifying features are observed for the control device, which exhibits a symmetric *I-V* relationship for all V_G polarities (Fig. 3d). The control device actually shows a typical *p*-channel transistor behaviour, where the conductance of the nanochannel is modulated by the field effect. In a negatively charged SiO_2 nanochannel, cations are the majority carriers, which are expected to increase or decrease when subjected to negative or positive electrostatic potentials, respectively. Therefore, the channel conductance will be enhanced at a negative V_G and suppressed at a positive V_G. From the comparison of the FERD and the control devices, we conclude that it is indeed the asymmetric positioning of the gate electrode that introduces the rectifying behaviour, whose favourable direction is not fixed but switchable via a gate potential.

Qualitative analysis. To understand the asymmetrical-gate controlled nanofluidic diodes, we developed a qualitative interpretation by looking at the change of the transient drift current of both cations and anions inside the nanochannel immediately after V_{CT} bias is applied with different V_G polarities (Fig. 4a). Because the ionic concentration distributions cannot change instantly, they remain the same as the steady state during this transient period. As a result, the diffusion current is not considered. The solid and empty bars inside the nanochannels in Figure 4a correspond to the cation and anion concentrations, respectively. The length of the bars depicts the amount of the ionic concentration as well as the drift current (because the drift current is linearly proportional to the ionic concentrations). According to the Kirchhoff's current law, the sum of currents flowing into any node should be equal to the sum of currents flowing out of that node, we get $J_C^K - J_C^{Cl} = J_T^K - J_T^{Cl}$. Therefore, the length sum of the two bars in each side of the channel should be equal.

When the gate potential is negative (upper row in Fig. 4a), the cation concentration immediately beneath the gate electrode is enhanced by the electrostatic attraction. With a negative V_{CT} (upper left panel, Fig. 4a), anions are driven towards the *Trans* side and the cations towards the *Cis* side, as indicated by the arrows. Under such a circumstance, the amount of the cation/anion flux flowing out of the centre junction of the nanochannel is larger than that flowing into it. As a result, when the system reaches the steady state again, the ions in the channel centre will be depleted, resulting in a depletion region with a lower conductance. Conversely, with a positive V_{CT} bias (upper right panel, Fig. 4a), the flow directions of the ions are reversed. More ions flow into the centre junction of the nanochannel while fewer ions flow out. This causes an accumulation of ions in the nanochannel and hence an increase of steady state conductance. Therefore, rectification of ionic transport is established and the preferential ionic current flow direction is from the *Cis* side to the *Trans* side when $V_G < 0$.

When a positive gate voltage is imposed (lower row in Fig. 4a), the cation concentration near the *Cis* side of the nanochannel is reduced by the electrostatic repulsion. Following the same analysis, it is obvious to conclude that a negative V_{CT} conducts more ionic current than a positive V_{CT} of the same magnitude. As a result, rectification of ionic current is also established, but the preferential ionic current direction is reversed as compared with the case of a negative gate potential.

Quantitative analysis. The quantitative analysis of the ion transport through the nanopores and nanochannels is generally calculated by concurrently solving the coupled Poisson–Nernst–Planck, and Navier–Stokes equations[36–40]. Since the contribution of electroosmosis is usually very small compared with the diffusive components, the Navier–Stokes equations can be neglected[40,41]. We calculated the steady-state distributions of cation/anion concentrations by self-consistently solving the coupled Poisson–Nernst–Planck equations. To take into account the field effect arising from the externally imposed gate potential, the electric potential inside the gate dielectric is also solved simultaneously (Supplementary Fig. S4 and Supplementary Methods). The calculated concentration profiles under different V_G and V_{CT} polarities are shown in Figure 4b. The quantitative steady state ion profile agrees well with the qualitative transient analysis in Figure 4a. The ion enrichment and depletion effect at the micro/nano channel interface[13] is also observed in the calculated results ($x = \pm 4\,\mu m$). This entrance effect contributes only a small portion of the total conductance and is not responsible for the field-effect-tunable rectifying property, as shown in Supplementary Figure S3.

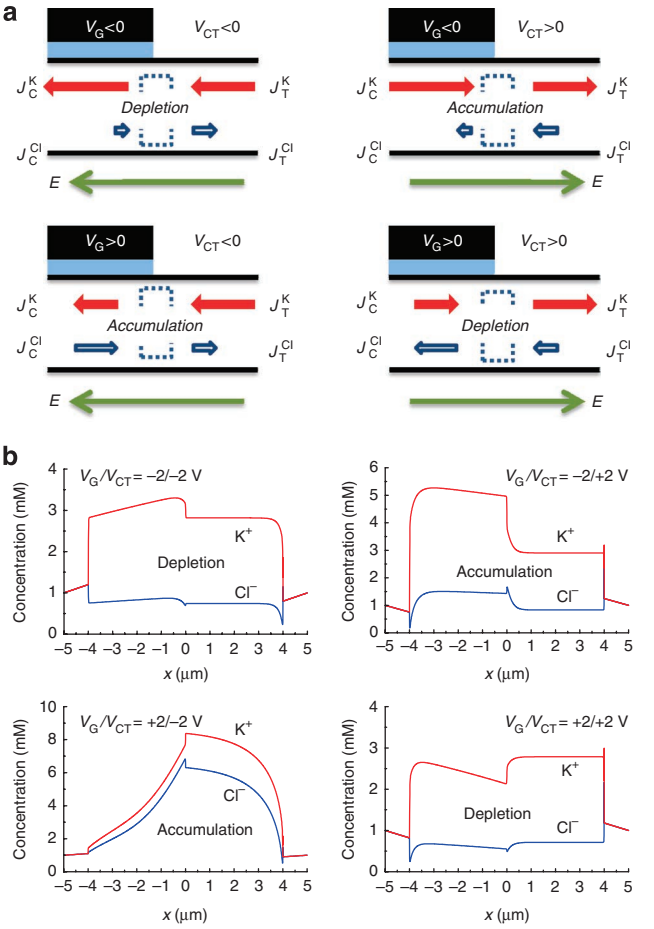

Figure 4 | Qualitative and quantitative analysis of the nanofluidic FERD. (**a**) Schematic diagram of cation and anion fluxes under various conditions. The solid red and the empty blue bars represent cation and anion concentrations as well as the corresponding current flux. The length of the bars depicts their amount (not to scale). The resulting ion depletion or accumulation taking place in the centre junction of the nanochannel at steady state can be obtained by comparing the amount of ion fluxes flowing into and away from the dashed box. (**b**) Quantitatively calculated steady state profiles of the ion concentrations along the channel length under different V_{CT} and V_G polarities at 1 mM KCl. The averaged K and Cl concentrations is calculated by $\langle c(x)\rangle = \int_{y=-H/2}^{y=H/2} c(x,y)dy/H$, where H is the channel height. The surface charge density used in the calculation is $\sigma_s = -2\,mC\,m^{-2}$.

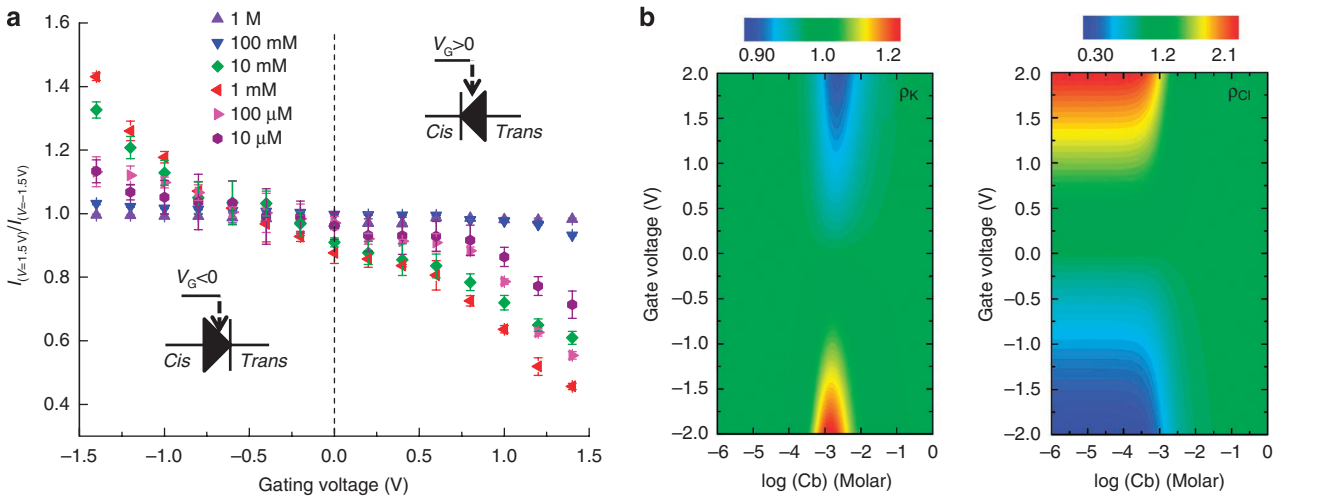

Figure 5 | Effect of the ionic concentrations on the rectifying degree under various gate potentials. (**a**) Experimental results. The error bars correspond to ten measurements. The inset symbols schematically show the forward direction switched with positive and negative gate voltages. (**b**) Calculated ratios of cation flux (ρ_K) and ratios of anion flux (ρ_{Cl}) via the *Cis* and *Trans* side of the nanochannel as a function of gate potential V_G and bulk concentration C_b. The surface charge density used in the calculation is $\sigma_s = -2\,mC\,m^{-2}$.

Concentration dependence of the rectifying behaviour. Interestingly, the field-effect reconfigurable rectifying behaviour shows a strong dependence on ionic concentrations. We recorded the I_{CT} as a function of V_{CT} for V_G ranging from negative to positive values at various KCl concentrations. The rectifying degree ($R = I_{+V}/I_{-V}$, where $V = 1.5\,V$) is plotted as a function of V_G (Fig. 5a). The voltage tunability of the FERD devices (that is, the slope of the R-V_G plot in Fig. 5a) becomes less prominent at both high and low KCl concentrations. With 1 M and 100 mM KCl solutions, no diode characteristics (asymmetric I–V curve) were observed experimentally. The most pronounced voltage tunability happens at intermediate KCl concentrations (1 mM and 10 mM). The qualitative trend that the tunable rectifying property being most prominent at intermediate ion concentrations and weakened at both low and high ionic concentrations is also observed in the numerical calculations (Supplementary Fig. S5). The rectifying degree shows a monotonically decreasing dependence on V_G when [KCl] < 100 mM. Consequently, the forward direction of the nanofluidic diode can be electrically switched by the application of an external gate potential (inset symbols of Fig. 5a), consistent with the results in Figures 3 and 4.

Another intriguing feature of Figure 5a is that, at a fixed gate voltage (for example, −1.5 V), the highest rectifying degree occurs at the intermediate ion concentrations rather than the lowest concentration regime where surface charge-governed ion conduction dominates. This counterintuitive phenomenon has also been observed in the systems of two terminal conical nanopore diodes[18], and nanochannel diodes[20–22,24,41]. However, a physical picture is lacking in understanding this behaviour.

Here we develop a physical model to explain these intriguing phenomena observed in our field-effect controlled diodes, with the aim to improve the rectification ratios. Referring to Figure 4a and considering the averaged concentrations of K and Cl ions at the two segments of the nanochannel, we denote the relation in the gated area (subscript C) and the un-gated area (subscript T) as $[K]_C = \gamma_C[Cl]_C$, and $[K]_T = \gamma_T[Cl]_T$, where γ is the cation/anion ratio. The cation/anion ratio can be determined through the electroneutrality and the law of conservation of mass as (Supplementary Methods), $\gamma_C = (-s_C + \sqrt{s_C^2 + 4C_b^2})^2/4C_b^2$ and $\gamma_T = (-s_T + \sqrt{s_T^2 + 4C_b^2})^2/4C_b^2$, where $S_C = (2\sigma_s - \varepsilon_0\varepsilon_{ox}V_g/d_{ox})/ehN_A$ and $S_T = 2\sigma_s/ehN_A$. ε_{ox} and d_{ox} are the permittivity and the thickness of dielectric SiO_2, respectively. By using the total current continuity at the micro/nano channel interfaces, we can obtain the ratios of cation (anion) flux via the *Cis* side over the cation (anion) flux via the *Trans* side of the nanochannel as (Supplementary Methods),

$$\rho_K = \frac{J_C^K}{J_T^K} = \frac{1+\gamma_C^{-1}}{1+\gamma_T^{-1}} \quad (1)$$

$$\rho_{Cl} = \frac{J_C^{Cl}}{J_T^{Cl}} = \frac{1+\gamma_C}{1+\gamma_T} \quad (2)$$

To observe a rectifying behaviour, $\rho_K \neq 1$ and $\rho_{Cl} \neq 1$ are required in the nanochannels (that is, the two solid bars, or the two empty bars in Figure 4a should be unequal in length). In fact, the further the value of ρ_K and ρ_{Cl} deviates from unity, the more pronounced is the rectification. Apparently, ρ_K or ρ_{Cl} is a function of V_G, C_b and σ_s, which is plotted in Figure 5b. At very high concentrations ($C_b > 100$ mM), the averaged ion concentrations in the nanochannel are dominated by the bulk rather than the surface and, hence, are barely affected by the external potential. Therefore, $\gamma_C \sim 1$ and $\gamma_T \sim 1$ (bulk property), which results in $\rho_K = \rho_{Cl} = 1$ and no rectifying behaviour would be observed. At very low concentrations ($C_b < 100\,\mu$M), we obtain $\rho_K \sim 1$ and $\rho_{Cl} \neq 1$. However, since K is the majority carrier that dominates the total ionic flux, the rectifying effect is less significant. At intermediate concentrations ($C_b \sim 1$ mM), where $\rho_K \neq 1$ and $\rho_{Cl} \neq 1$, the most profound rectifying behaviour is expected.

Discussion

The above analysis implies the strategies that can be adopted to improve the gate-tunable rectifying effect. Higher rectifying effect will happen when $\gamma_C \ll 1 \ll \gamma_T$ or $\gamma_T \ll 1 \ll \gamma_C$. For an intrinsically negatively charged nanochannel SiO_2 wall, it is obvious that $\gamma_T \gg 1$. To achieve $\gamma_C \ll 1$, the charge polarity beneath the gate electrode needs to be reversed, which requires $\varepsilon_0\varepsilon_{ox}V_g/d_{ox} > 2|\sigma_s|$. Take $\sigma_s = -2\,mC\,m^{-2}$, for example, the minimal gate voltage required for charge polarity reversal is about 9 V. This is inaccessible in our current devices owing to the gate leakage and breakdown limitations (Supplementary Fig. S6). However, if a surround-gate architecture (that is, with both the top gate and the back gate) is used, the minimal gate voltage needed to reverse the charge polarity would be reduced by half. In addition, for a better control over cation/anion ratios, a low surface charge density is desirable. This is because an inherent high surface charge density in nanochannels resembles degenerate doping in a semiconductor or high surface state density of a FET,

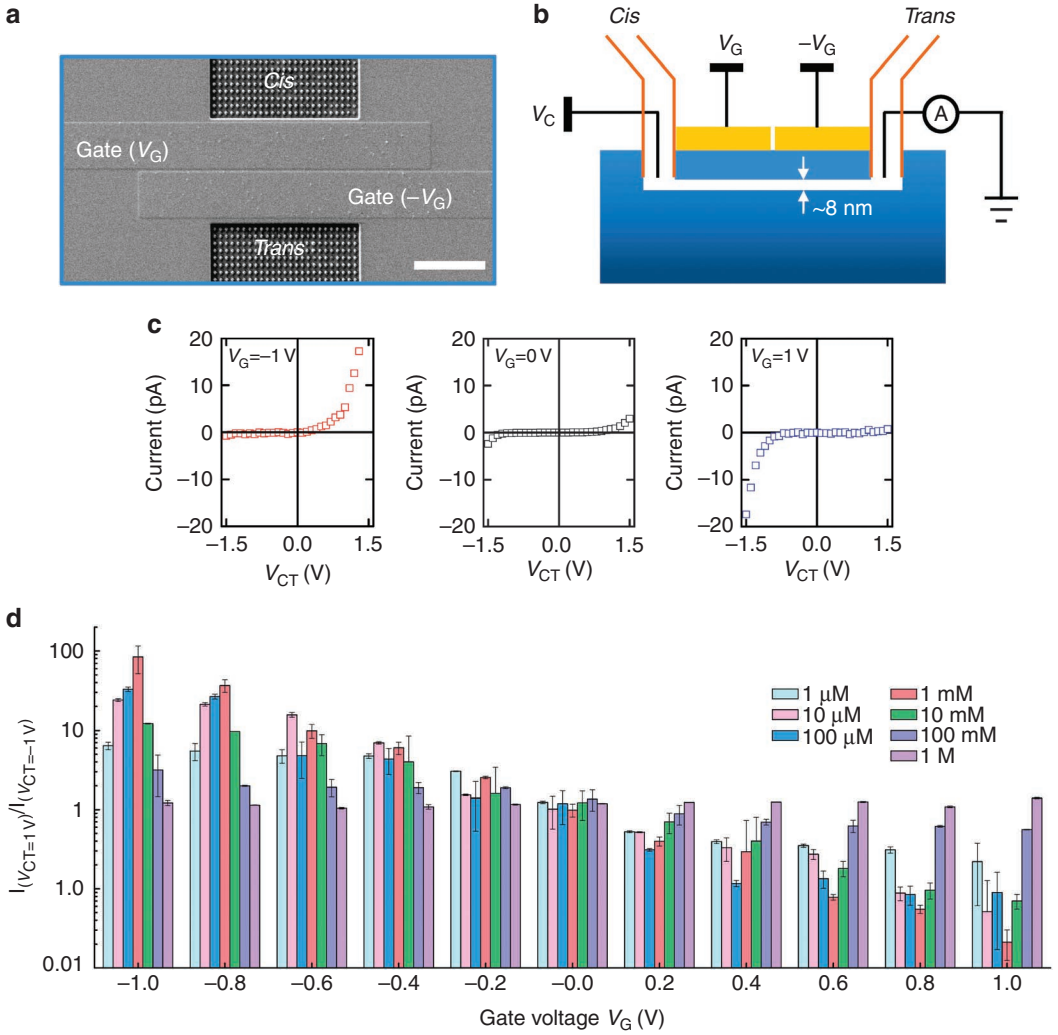

Figure 6 | Improved field-effect tunability over the ionic diode property with devices of a dual split-gate structure. (**a**) SEM image of the dual split-gate FERD devices (W = 1 μm×11, L = 116 μm, H = 8 nm). The scale bar is 100 μm. The nanochannel wall is chemically modified to be less charged and hydrophilic. The separation between the two gates is 4 μm. (**b**) Testing configurations for the dual gate FERD device. (**c**) Typical I_{CT}-V_{CT} curves at different gate voltages V_G (−1 V, 0 V, +1 V), for a given ionic concentration (1 mM). (**d**) Measured rectifying degree (referenced at V_{CT} = ±1 V) as a function of V_G for KCl concentrations ranging from 1 μM to 1 M.

making the electrostatic control of the ionic concentrations in the nanochannel difficult[6]. By neutralizing the intrinsic surface charge through chemical modifications, it would allow for more efficient gate modulation in the *Cis* side. A separate gate on top of the *Trans* segment would further permit the cation/anion modulation in the *Trans* side. Therefore, by placing dual gate electrodes along the channel length, one can have more flexibility to tune the rectifying property via the dual gates. Moreover, reducing the nanochannel dimensions down to sub-10 nm would allow the diodes to function at a more realistic ionic concentrations (for example, physiological conditions, ~10–100 mM)[7]. To sum up, an ideal structure for field-effect reconfigurable nanofluidic diodes would be dual split-gates with a gate-all-around structure and a sub-10 nm nanochannels of a neutral surface.

To experimentally verify these predictions, we fabricated another wafer of devices with a dual gate structure (Fig. 6a) and an 8-nm-thick nanochannel (determined by the thickness of the sacrificial Cr layer). The surface charge of the as-fabricated nanochannel is estimated as $\sigma_s = -1.6\,mC\,m^{-2}$ (Supplementary Fig. S7). This native surface charge density is reduced by sequentially treating the nanochannel wall with 3-Glycidoxypropyltrimethoxysilane and ethanolamine (Supplementary Methods). The resulting nanochannel surface is highly hydrophilic and the modified surface charge is estimated as $\sigma_s = -0.3\,mC\,m^{-2}$ (Supplementary Fig. S7). With this surface-modified dual-gate device and an electrical setup schematically shown in Figure 6b, we recorded the I_{CT} as a function of V_{CT} for V_G ranging from negative to positive values at various KCl concentrations. Figure 6c shows typical I_{CT}-V_{CT} curves at different gate voltages V_G, for a given ionic concentration (1 mM). The rectifying ratio ($R = I_{+V}/I_{-V}$, where V = 1 V) is plotted as a function of V_G for seven different KCl concentrations (Fig. 6d). The dual-gate device with the chemically modified surface shows a tremendously improved rectification ratio. At $V_G = -1$ V, the rectification ratio reaches ~83 for 1 mM KCl, much higher than that of the single-gate device shown in Figure 5a (a ratio of ~1.2 under the same conditions). We note that the rectification ratio can be even higher under larger reference V_{CT} biases. Interestingly, the dual-gate device also exhibits a higher rectifying degree at the intermediate ion concentrations under a fixed gate voltage (for example, $V_G = -1$ V in Fig. 6d).

In conclusion, we propose and demonstrate a field-effect reconfigurable nanofluidic diode based on an asymmetric field effect. This general concept could conceivably be applied to similar thin-body solid-state devices (for example, silicon-on-insulator or semiconducting nanowire). Compared with any existing nanofluidic control

systems including stimuli-responsive tuning, the electrostatic modulation platform offers the full potential for logical programming of rectified transport of ionic and molecular species. Unlike the nanofluidic field-effect transistor, where only the amount of ions/molecules is regulated by an electrostatic potential, the FERD can be used to control both directions and magnitudes of ion/molecule transport. FERD represents a fundamentally novel system and may function as the building block to create an on-demand, reconfigurable, large-scale integrated nanofluidic circuits for digitally programmed manipulation of biomolecules such as polynucleotides and proteins.

Methods

Device fabrication. We used a sacrificial layer method to produce the nanochannels. However, there is a major difference in our process. The conventional method etches the sacrificial layer first and then integrates the nanochannel device with a microfluidic interface to form a functional device[22,24,42]. We find that the nanochannels fabricated by this method are inclined to collapse because of the capillary force in the drying process and/or the pressure exerted during the bonding process. To overcome this problem, we developed a novel 'bond-followed-by-etch' scheme. Briefly, 11 thin Cr stripes are patterned on top of an insulating SiO_2 layer on a 4-inch silicon wafer. Then a dielectric SiO_2 layer (50-nm-thick) is subsequently deposited by plasma enhanced chemical vapour deposition, followed by a rapid thermal annealing process to improve the dielectric quality. Gate electrode is thereafter formed by a double layer lift-off process. The accessing reservoirs with supporting pillars are etched simultaneously by reactive CHF_3/Ar plasma at a rate of 1 nm s^{-1}. The device is then aligned and permanently bonded with a microfluidic polydimethylsiloxane stamp. The Cr etchant is pumped into the microchannel afterwards, which diffusively etches the Cr sacrificial layer *in situ*. The end-point detection for the etching process is done by looking at the colour contrast under a microscope. Deionized water is flushed through the microchannel after the etching process is finished, and then the device is ready to use. As neither the drying process nor the external pressure is applied, the 'bond-followed-by-etch' scheme completely avoids the nanochannel collapse problem. Moreover, the top-down process results in a uniform nanochannel dimensions along the length the channels and across the array.

Electrical characterization. The whole testing procedure is done using an automatic system. The solutions are delivered by pumps (New Era Pump Systems), controlled by a LabVIEW program (National Instruments). The current-voltage measurement is performed using HP4156B semiconductor parameter analyzer and is synchronized with the pump by the same LabVIEW program. Data post-processing is done with MATLAB (The MathWorks) software.

Numerical calculation. The steady-state distributions of the cation/anion concentration and the ionic current under different V_G and V_{CT} biases are calculated by solving the coupled two-dimensional Poisson–Nernst–Planck equations within the COMSOL script environment. We use three modules in the COMSOL environment: Electrostatics (AC/DC Module), Nernst–Planck without electroneutrality for the calculation of K^+ ions (Chemical Engineering Module) and Nernst–Planck without electroneutrality for the calculation of Cl^- ions (Chemical Engineering Module). The simulation system contains an 8-μm-long, 20-nm-high nanochannel that is connected by two 1×1 μm^2 square reservoirs. The SiO_2 dielectric is 50-nm-thick and 4-μm-long, with surface charge density as $\sigma_s = -2\,mC\,m^{-2}$. The length of the nanochannel used for calculation is less than the real device (100 μm) to reduce the simulation time.

References

1. van den Berg, A., Craighead, H. G. & Yang, P. D. From microfluidic applications to nanofluidic phenomena. *Chem. Soc. Rev.* **39,** 899–900 (2010).
2. Smith, P. L., Baukrowitz, T. & Yellen, G. The inward rectification mechanism of the HERG cardiac potassium channel. *Nature* **379,** 833–836 (1996).
3. Gajar, S. A. & Geis, M. W. An ionic liquid-channel field-effect transistor. *J. Electrochem. Soc.* **139,** 2833–2840 (1992).
4. Fan, R., Yue, M., Karnik, R., Majumdar, A. & Yang, P. D. Polarity switching and transient responses in single nanotube nanofluidic transistors. *Phys. Rev. Lett.* **95,** 086607 (2005).
5. Karnik, R. *et al.* Electrostatic control of ions and molecules in nanofluidic transistors. *Nano Lett.* **5,** 943–948 (2005).
6. Karnik, R., Castelino, K. & Majumdar, A. Field-effect control of protein transport in a nanofluidic transistor circuit. *Appl. Phys. Lett.* **88,** 123114 (2006).
7. Fan, R., Huh, S., Yan, R., Arnold, J. & Yang, P. D. Gated proton transport in aligned mesoporous silica films. *Nat. Mater.* **7,** 303–307 (2008).
8. Nam, S. W., Rooks, M. J., Kim, K. B. & Rossnagel, S. M. Ionic field effect transistors with sub-10 nm multiple nanopores. *Nano Lett.* **9,** 2044–2048 (2009).
9. Joshi, P. *et al.* Field effect modulation of ionic conductance of cylindrical silicon-on-insulator nanopore array. *J. Appl. Phys.* **107,** 054701, 1–6 (2010).
10. Maglia, G. *et al.* Droplet networks with incorporated protein diodes show collective properties. *Nat. Nanotech.* **4,** 437–440 (2009).
11. Ali, M., Mafe, S., Ramirez, P., Neumann, R. & Ensinger, W. Logic gates using nanofluidic diodes based on conical nanopores functionalized with polyprotic acid chains. *Langmuir* **25,** 11993–11997 (2009).
12. Vlassiouk, I., Kozel, T. R. & Siwy, Z. S. Biosensing with nanofluidic diodes. *J. Am. Chem. Soc.* **131,** 8211–8220 (2009).
13. Kim, S. J., Song, Y. A. & Han, J. Nanofluidic concentration devices for biomolecules utilizing ion concentration polarization: theory, fabrication, and applications. *Chem. Soc. Rev.* **39,** 912–922 (2010).
14. Kim, S. J., Ko, S. H., Kang, K. H. & Han, J. Direct seawater desalination by ion concentration polarization. *Nat. Nanotech.* **5,** 297–301 (2010).
15. Cheng, L. J. & Guo, L. J. Nanofluidic diodes. *Chem. Soc. Rev.* **39,** 923–938 (2010).
16. Wei, C., Bard, A. J. & Feldberg, S. W. Current rectification at quartz nanopipet electrodes. *Anal. Chem.* **69,** 4627–4633 (1997).
17. Siwy, Z. *et al.* Rectification and voltage gating of ion currents in a nanofabricated pore. *Europhys. Lett.* **60,** 349–355 (2002).
18. Cervera, J., Schiedt, B., Neumann, R., Mafe, S. & Ramirez, P. Ionic conduction, rectification, and selectivity in single conical nanopores. *J. Chem. Phys.* **124,** 104706, 1–9 (2006).
19. Perry, J. M., Zhou, K. M., Harms, Z. D. & Jacobson, S. C. Ion transport in nanofluidic funnels. *ACS Nano* **4,** 3897–3902 (2010).
20. Cheng, L. J. & Guo, L. J. Ionic current rectification, breakdown, and switching in heterogeneous oxide nanofluidic devices. *ACS Nano* **3,** 575–584 (2009).
21. Yan, R. X., Liang, W. J., Fan, R. & Yang, P. D. Nanofluidic diodes based on nanotube heterojunctions. *Nano Lett.* **9,** 3820–3825 (2009).
22. Karnik, R., Duan, C. H., Castelino, K., Daiguji, H. & Majumdar, A. Rectification of ionic current in a nanofluidic diode. *Nano Lett.* **7,** 547–551 (2007).
23. Miedema, H. *et al.* A biological porin engineered into a molecular, nanofluidic diode. *Nano Lett.* **7,** 2886–2891 (2007).
24. Cheng, L. J. & Guo, L. J. Rectified ion transport through concentration gradient in homogeneous silica nanochannels. *Nano Lett.* **7,** 3165–3171 (2007).
25. Vlassiouk, I. & Siwy, Z. S. Nanofluidic diode. *Nano Lett.* **7,** 552–556 (2007).
26. Alcaraz, A. *et al.* A pH-tunable nanofluidic diode: Electrochemical rectification in a reconstituted single ion channel. *J. Phys. Chem. B* **110,** 21205–21209 (2006).
27. Yameen, B. *et al.* Proton-regulated rectified ionic transport through solid-state conical nanopores modified with phosphate-bearing polymer brushes. *Chem. Commun.* **46,** 1908–1910 (2010).
28. Ali, M., Ramirez, P., Mafe, S., Neumann, R. & Ensinger, W. A pH-Tunable nanofluidic diode with a broad range of rectifying properties. *ACS Nano* **3,** 603–608 (2009).
29. Macrae, M. X., Blake, S., Mayer, M. & Yang, J. Nanoscale ionic diodes with tunable and switchable rectifying behavior. *J. Am. Chem. Soc.* **132,** 1766–1767 (2010).
30. He, Y. *et al.* Tuning transport properties of nanofluidic devices with local charge inversion. *J. Am. Chem. Soc.* **131,** 5194–5202 (2009).
31. Schoch, R. B. & Renaud, P. Ion transport through nanoslits dominated by the effective surface charge. *Appl. Phys. Lett.* **86,** 253111 (2005).
32. Stein, D., Kruithof, M. & Dekker, C. Surface-charge-governed ion transport in nanofluidic channels. *Phys. Rev. Lett.* **93,** 035901 (2004).
33. Behrens, S. H. & Grier, D. G. The charge of glass and silica surfaces. *J. Chem. Phys.* **115,** 6716–6721 (2001).
34. Schoch, R. B., Han, J. Y. & Renaud, P. Transport phenomena in nanofluidics. *Rev. Mod. Phys.* **80,** 839–883 (2008).
35. Sze, S. M. *Physics of Semiconductor Devices* 2nd edn (John Wiley and Sons, 1981).
36. Daiguji, H., Oka, Y. & Shirono, K. Nanofluidic diode and bipolar transistor. *Nano Lett.* **5,** 2274–2280 (2005).
37. Daiguji, H., Yang, P. D. & Majumdar, A. Ion transport in nanofluidic channels. *Nano Lett.* **4,** 137–142 (2004).
38. Constantin, D. & Siwy, Z. S. Poisson-Nernst -Planck model of ion current rectification through a nanofluidic diode. *Phys. Rev. E* **76,** 041202 (2007).
39. Kalman, E. B., Vlassiouk, I. & Siwy, Z. S. Nanofluidic bipolar transistors. *Adv. Mater.* **20,** 293–297 (2008).
40. Vlassiouk, I., Smirnov, S. & Siwy, Z. Ionic selectivity of single nanochannels. *Nano Lett.* **8,** 1978–1985 (2008).
41. Vlassiouk, I., Smirnov, S. & Siwy, Z. Nanofluidic ionic diodes. Comparison of analytical and numerical solutions. *ACS Nano* **2,** 1589–1602 (2008).
42. Karnik, R., Castelino, K., Fan, R., Yang, P. & Majumdar, A. Effects of biological reactions and modifications on conductance of nanofluidic channels. *Nano Lett.* **5,** 1638–1642 (2005).

Acknowledgements

We thank Nitin Rajan for the help of electrical characterization as well as useful discussions, and Michael Power for the help during the device fabrication process. W.G. acknowledges the support from Howard Hughes Medical Institute International Student Research Fellowship.

Author contributions

W.G. conceived the concept and designed the experiments. M.A.R. supervised the study. W.G. carried out the experiment and, together with R.F. analysed the data. W.G. and M.A.R. co-wrote the manuscript and discussed it with R.F.

Additional information

Supplementary Information accompanies this paper at http://www.nature.com/naturecommunications

Competing financial interests: The authors declare no competing financial interests.

Reprints and permission information is available online at http://npg.nature.com/reprintsandpermissions/

How to cite this article: Guan W. *et al.* Field-effect reconfigurable nanofluidic ionic diodes. *Nat. Commun.* 2:506 doi: 10.1038/ncomms1514 (2011).

Supplementary Figures

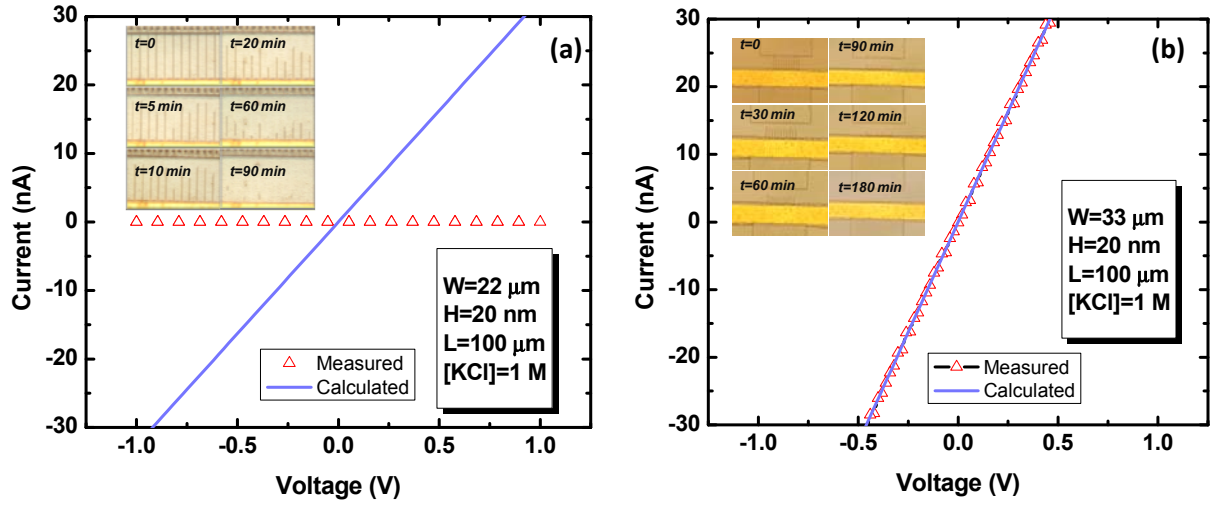

Supplementary Figure S1 | Comparison between the two different sacrificial layer etching schemes. **(a)** The current-voltage (I-V) curve for the device fabricated using 'etch and bond' scheme. The inset shows the etching process monitored under the microscope. The measured current is in the order of pico-ampere (pA) and falls very short of the calculated current, which strongly implies a clogged nanochannel. The reasons for the nanochannel collapse may come from two factors, which are the capillary force in the drying process and the pressure exerted during the PDMS bonding process. **(b)** The current-voltage (I-V) curve for the devices fabricated using 'bond followed by etch' scheme. The inset shows the sacrificial layer etching process monitored under the microscope. The measured current agrees very well with calculated current. This confirms the success of the 'bond followed by etch' scheme.

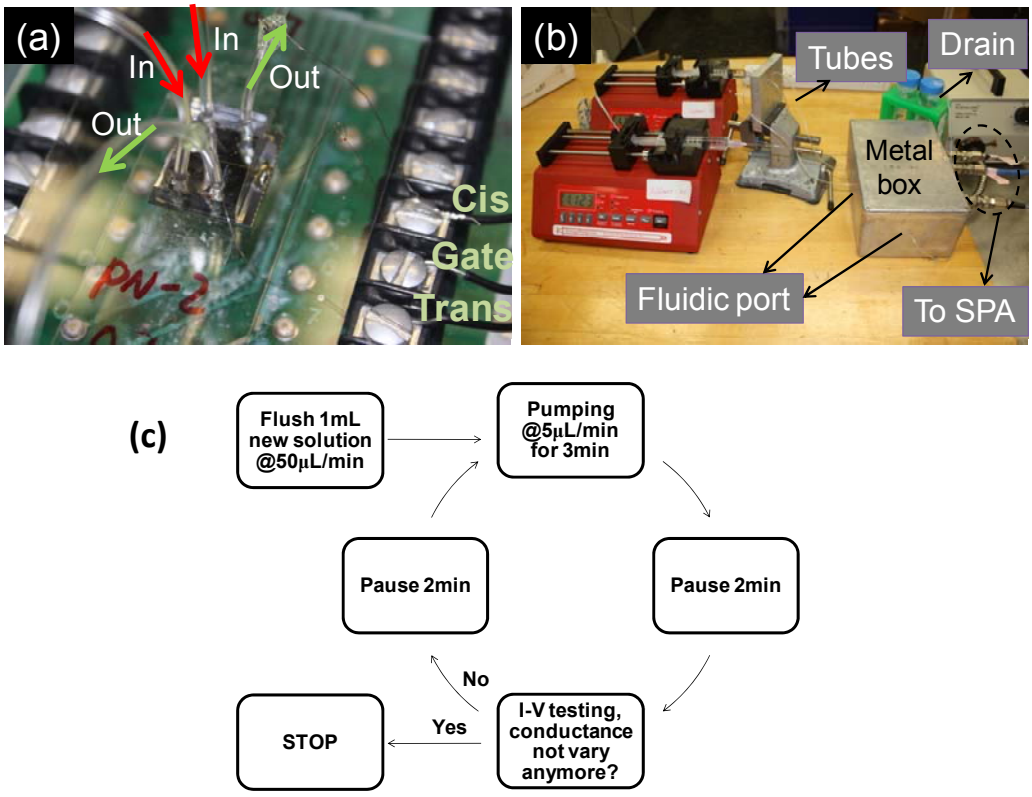

Supplementary Figure S2 | Experimental setup and schemes of electrical measurements. (a) The functional device is wire bonded onto a printed circuit board (PCB). The Ag/AgCl electrodes are integrated with the connecting tubes, serving as a low resistive loss contact. **(b)** The whole PCB board is housed inside a light-shielding metal box. The metal box has maximal four BNC connectors (for connection to Cis, Trans and Gate terminals) and four small holes for tubing entering. This setup minimizes the noise from the environment. The whole testing procedure is done using an automatic system. The solutions are delivered by pumps (New Era Pump Systems, Inc) which are controlled by a LabVIEW (National Instruments) program. The current-voltage (I-V) characteristics are measured using HP4156B semiconductor parameter analyzer (SPA). **(c)** Procedure for determining the equilibrium state of a newly introduced solution. When changing concentrations from one value to the other, we always monitor the conductance between the Cis and Trans reservoirs with gate terminal floating. The conductance is determined by a linear fit of the measured current as a function of voltage, scanning from -1 V to 1 V (with a voltage step of 0.1 V and a delay time of 3 s between each measurement point). The equilibrium state for the new solution is reached when the conductance is not changing anymore. And the corresponding experiments are only carried out after this equilibrium state.

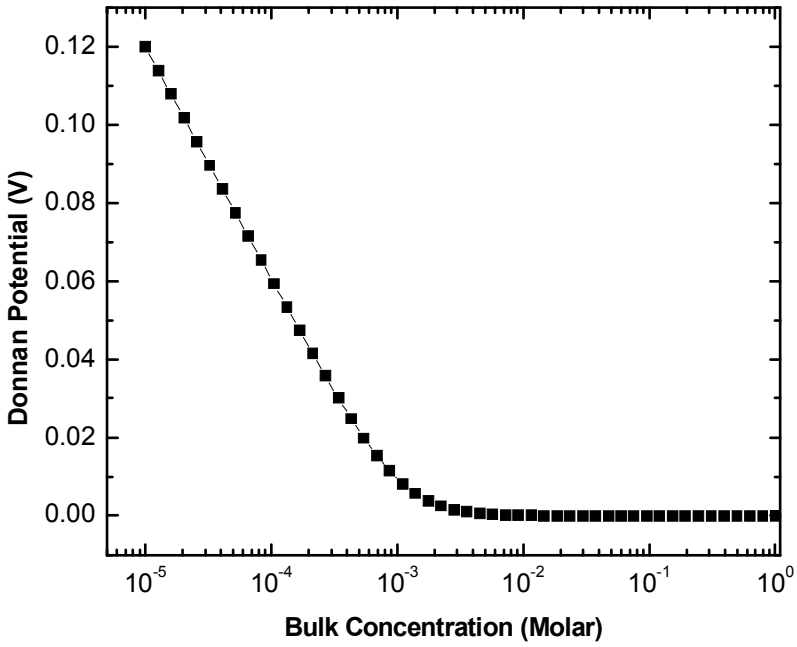

Supplementary Figure S3 | **The Donnan potential barrier as function of bulk concentration.** When a charge-selective nanochannel is in equilibrium with an adjacent microfluidic reservoir, the electrochemical potentials of the cation (K) or anion (Cl) should be equal in both nanochannels and microchannels. This electrochemical equilibrium is referred to as the Donnan equilibrium. An analogy in semiconductor devices is the aligned Fermi-level. When the Donnan equilibrium of counterions is attained at the microchannel/nanochannel interface, this leads to the Donnan barrier potential at the interface and can be expressed as [34], $V_{bi} = \frac{RT}{F}\ln\frac{[Cl]_n}{C_b} = \frac{RT}{F}\ln\frac{\sqrt{4C_b^2 + s_n^2} + s_n}{2C_b}$, where R [J/(K·mol)] is the universal gas constant, T [K] is the absolute temperature, F [C/mol] is the Faraday constant, C_b [mol/m^3] is the bulk concentration. $s_n = 2\sigma_s / ehN_A$ is the nanochannel surface charge density averaged over the channel volume, and σ_s is the surface charge density (-2 mC/m^2), h is the nanochannel height (20 nm), N_A [mol^{-1}] is the Avogadro constant. It can be seen that at high concentrations (>1 mM), this barrier potential is negligible. The maximal barrier happens at low ionic concentrations and is about 0.12 V when the bulk concentration is 10 μM. As a result, this interfacial barrier is a negligible effect in the FERD devices and is not responsible for the voltage tunable rectifying property.

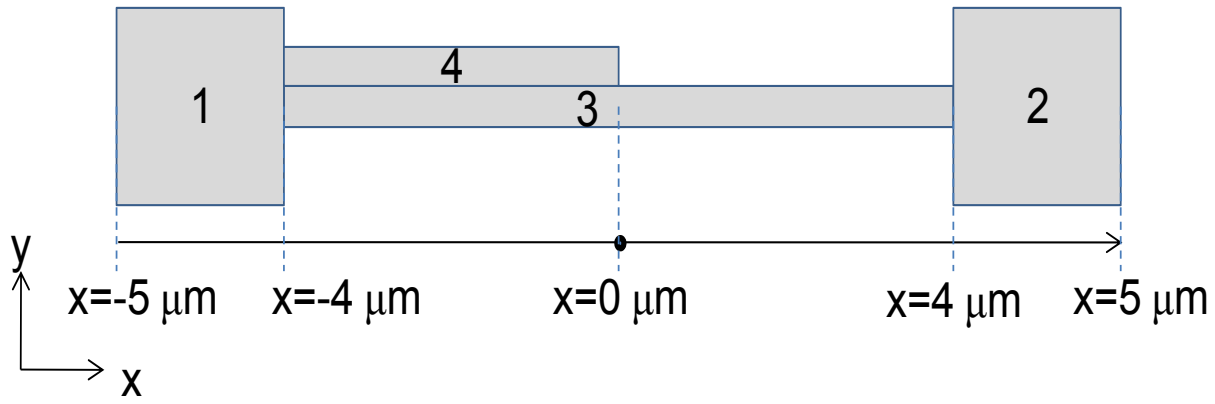

Supplementary Figure S4 | Simulation system used in the numerical calculation. It contains an 8-μm-long, 20-nm-high nanochannel (domain 3) connected by two 1×1 μm^2 square reservoirs (domain 1 and 2). In addition, there is a SiO_2 dielectric domain (domain 4) which is 50-nm-thick and 4-μm-long. The length of the nanochannel used for calculation is less than the real device (100 μm) in order to reduce the simulation time. Note the figure is not drawn to scale.

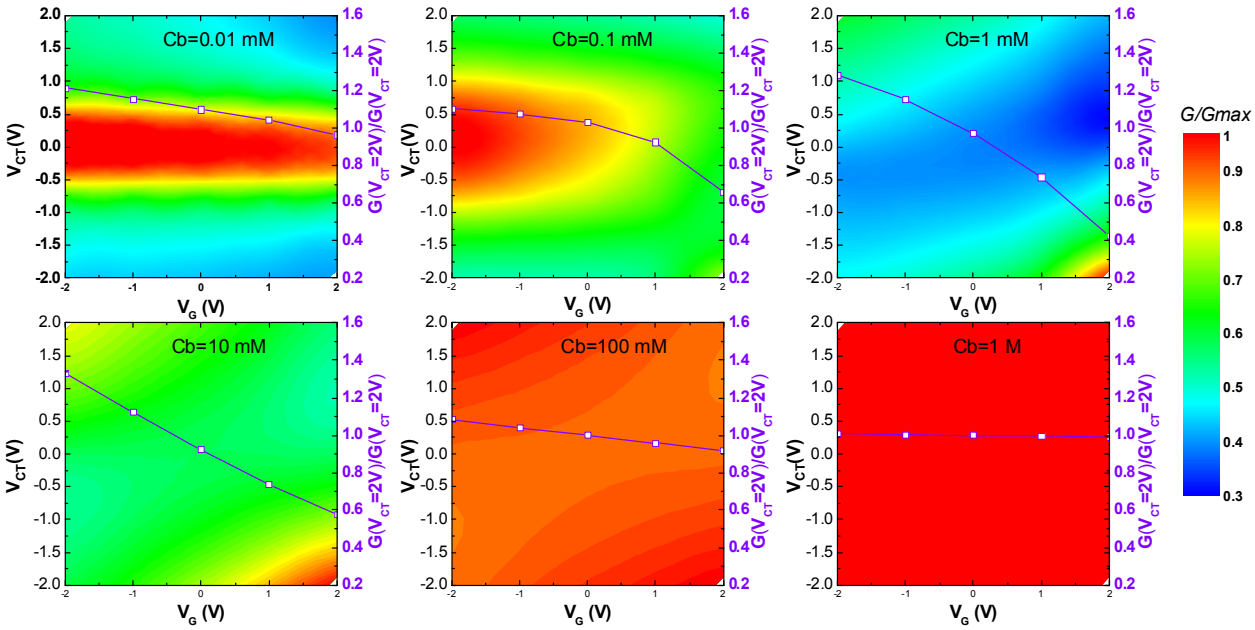

Supplementary Figure S5 | Normalized nanochannel conductance (G/G_{max}) as a function of V_G and V_{CT} for various bulk concentrations (C_b). The inset lines are the rectifying ratio at V_{CT}=±2 V. The asymmetry of the surface plot about the V_{CT}=0 indicates a rectifying property. It can be seen that the gate voltage tunable rectifying property is most prominent at intermediate ion concentrations (e.g. 1 mM and 10 mM), and is weakened at both low and high ionic concentrations. The general dependence of the rectifying degree on the gate potential and the bulk concentrations agrees very well with the experimental data shown in Figure 5 in the main text.

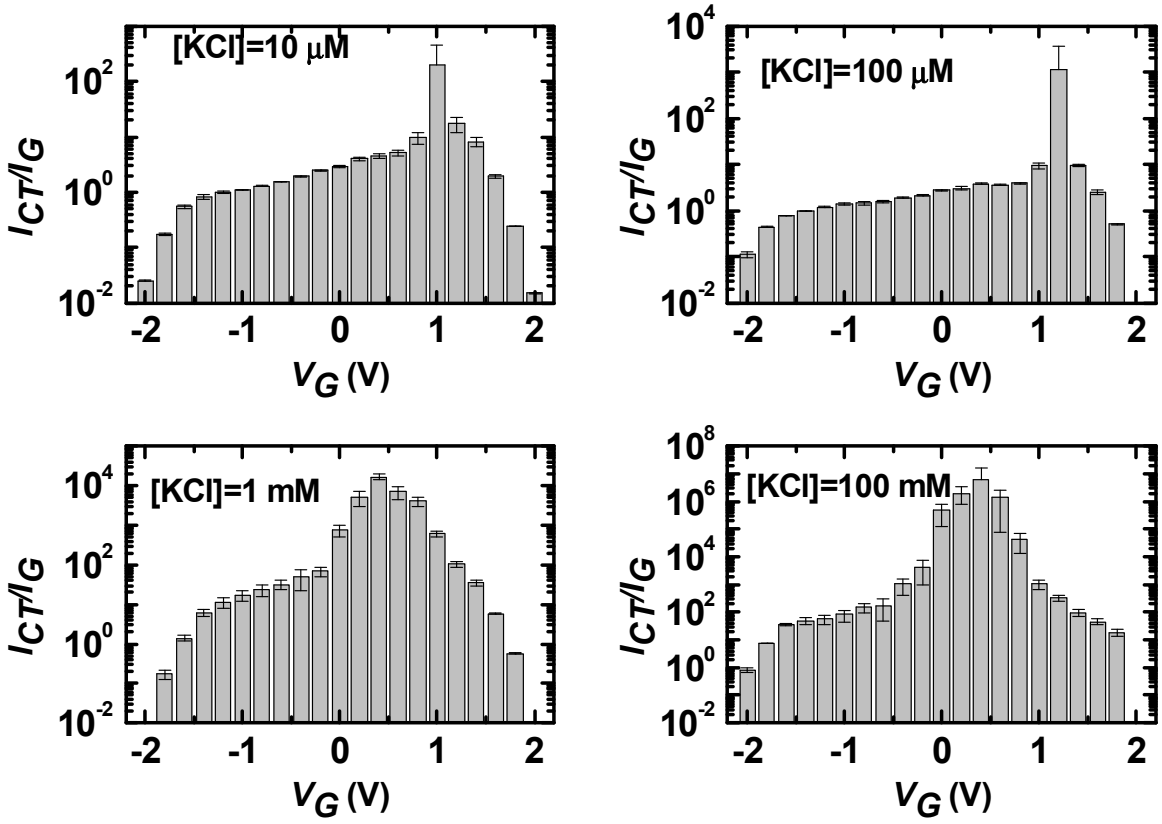

Supplementary Figure S6 | Gate Leakage considerations. Besides the capacitive coupling between the gate electrodes and the liquid nanochannel, the real dielectric is lossy and therefore a leakage current usually exists. We always monitor the gate leakage current (I_G) during the measurement. The figure of merit that we use to tell whether the gating effect is dominated by capacitive coupling or leakage coupling is by looking at the ratio of I_{CT} over I_G. If this ratio is less than 1, then the device has a significant amount of leakage current through the gate dielectric. To obtain a trustable capacitive gating results, we need I_{CT}/I_G to be larger than 1. This ratio is both gate voltage dependent and KCl concentration dependent. At high KCl concentrations, I_{CT}/I_G is usually very large because of the large I_{CT} flowing in the channel. However, at low KCl concentrations, the leakage current flowing between the nanochannel and the gate electrode can exceed I_{CT}. Nevertheless, I_{CT}/I_G is usually larger than 1 when the gate voltage is bounded between -1.5 V and 1.5 V, and this is a typical safe gate voltage range used in our experiments. The error bar corresponds to 10 measurements.

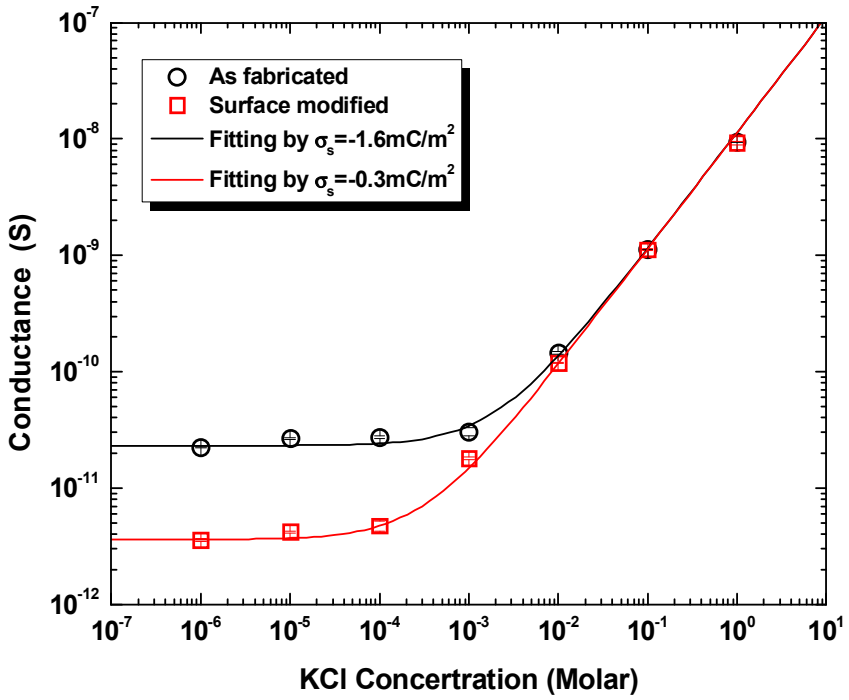

Supplementary Figure S7 | Measured conductance as a function of KCl concentrations for the nanochannel before and after surface modification. This dimensions for this nanochannel are *W*=11 μm, *L*=116 μm, *H*=8 nm. The surface charge is reduced from an intrinsic value of -1.6 mC/m^2 to -0.3 mC/m^2 after the modification.

Supplementary Table

Supplementary Table S1. Parameters used in the numerical simulation.

Parameters	Meaning	Value	Unit
ε_0	Vacuum permittivity	8.85e-12	F/m
ε_{SiO_2}	PECVD SiO_2 dielectric constant [43]	5	No unit
ε_w	KCl solution dielectric constant [44]	70	No unit
σ_s	Intrinsic surface charge	-2e-3	C/m^2
φ	Potentials in gate dielectric		V
c_i	Concentration of ionic species *i*		mol/m^3
C_b	Bulk concentration	Variables	mM
D_i	Diffusion coefficient	1.96e-9 (K^+), 2.03e-9 (Cl^-)	m^2/s
F	Faraday constant	96485.3415	s·A/mol
i	Ion species	1 (K^+), 2 (Cl^-)	No unit
I	Total current		A/m
I_i	Ionic current of i^{th} species		A/m
n	Normal vector		
N_i	Mass flux density of i^{th} species		$mol/(m^2 \cdot s)$
u_i	Ionic mobility of i^{th} species	7.62e-8 (K^+), 7.92e-8 (Cl^-)	$m^2/(V \cdot s)$
V	Potentials in the liquid		V
V_C	Potential in the Cis reservoir	variables	V
V_T	Potential in the Trans reservoir	variables	V
V_G	Gate potential	variables	V
z_i	Charge number	+1 (K^+), -1(Cl^-)	No unit

Supplementary Methods

'Etch and bond' approach

In this approach, the diced devices are firstly immersed in a chrome etchant solution (Transene, type 1020) heated at 70 °C, and the etching process is monitored under a microscope. A total time of 90 min is enough to remove the entire Cr sacrificial layer (vertical lines in the inset image of Supplementary Figure S1a). After the Cr layer is etched away, the device is rinsed with de-ionized (DI) water and dried in an oven. After that the surface of both the device and the PDMS stamp are treated with oxygen plasma and they are bonded together. It is during this bonding process that a certain pressure is needed to press these two pieces together. After the device is integrated, we carry out experiments to see whether the nanochannel functions correctly. 1 M KCl solutions are introduced into the microchannels and the Cis to Trans current is measured as a function of Cis to Trans voltage (Supplementary Figure S1a).

'Bond followed by etch' approach

To overcome the collapse problem encountered in the 'etch and bond' approach, we develop a new scheme to remove the sacrificial layer. The diced device and the PDMS stamp are firstly treated with oxygen plasma. Then we bond these two pieces together. Connecting tubes are inserted into PDMS inlet and outlet ports. Subsequently, DI water is pumped along the microchannel to wet the Cis/Trans reservoirs. Then the chrome etchant (Transene, type 1020) is pumped along the microchannel and it diffusively etches the embedded sacrificial Cr layer *in situ*. The inset images of Supplementary Figure S1b shows the etching process using this new approach. After the etching process being completed, DI water is flushed along the microchannels to rinse the channel. 1 M KCl solutions are introduced into the device and the I-V properties between the Cis and Trans reservoirs are tested (Supplementary Figure S1b).

Determination of the surface charge density

The conductance of a nanochannel filled with KCl solutions is the superposition of the bulk conductance $e(\mu_K+\mu_{Cl})C_bN_AWH/L$ and the double layer conductance $2\mu_K\sigma_SW/$L, where W [m], L [m] and H [m] are the width, length and height of the nanochannels, respectively. μ_K [$m^2/(V\cdot s)$] and μ_{Cl} [$m^2/(V\cdot s)$] are the mobility of K and Cl ions. C_b [mol/m^3] is the bulk concentration. N_A [mol^{-1}] is the Avogadro constant, e [C] is the elementary charge. σ_S [C/m^2] is the surface charge on the nanochannel walls. By knowing the

dimensions of the lithographically defined channels (*W, L*), we can derive the value of *H* in high concentration regime (bulk conductance part) and the value of surface charge σ_S in low concentration regime (double layer conductance part) by fitting the experimental data.

Numerical calculation

The steady-state distributions of the cation/anion concentration and the ionic current under different V_G and V_{CT} biases are calculated by solving the coupled two dimensional (2D) Poisson-Nernst-Planck (PNP) equations using COMSOL script environment. Supplementary Figure S4 shows the system that we use in the simulation.

We use three modules in the COMSOL environment: Electrostatics (AC/DC Module), Nernst-Planck without electroneutrality for calculation of K^+ ions (Chemical Engineering Module) and Nernst-Planck without electroneutrality for calculation of Cl^- ions (Chemical Engineering Module). The governing equations and the corresponding boundary conditions are listed as follows (Supplementary Table S1 summarizes all the parameters used in the simulation),

A. Electrostatics

(1) Governing equations (Poisson equation):

$\varepsilon_0\varepsilon_w\nabla^2 V = -\sum_i Fz_i c_i$ for domain 1, 2 and 3, and

$\varepsilon_0\varepsilon_{SiO_2}\nabla^2\varphi = 0$ for domain 4.

(2) Boundary conditions:

The Dirichlet boundary condition is used for the potentials at the ends of the two reservoirs, $V(x=-5\mu m)=V_C$ and $V(x=5\mu m)=V_T$. The gate electrode (top side of domain 4) has Dirichlet boundary condition as $V=V_G$. Neumann boundary conditions are applied for all the other reservoir walls, $-\varepsilon_0\varepsilon_w n\cdot\nabla V=0$. The nanochannel walls which are not in contact with the gate dielectric have the boundary condition as $-\varepsilon_0\varepsilon_w n\cdot\nabla V=\sigma_s$. The Neumann boundary condition is imposed on the interface between the gate dielectric and nanochannel as $-\varepsilon_0\varepsilon_w n\cdot\nabla V+\varepsilon_0\varepsilon_{SiO_2} n\cdot\nabla\varphi=\sigma_s$.

B. Steady state Nernst-Planck equation for either K^+ or Cl^-

(1) Governing equations:

$\nabla \cdot N_i = \nabla \cdot (-D_i \nabla c_i - z_i u_i c_i \nabla V) = 0$ for domain 1, 2 and 3, and inactive in domain 4.

(2) Boundary conditions:

The Dirichlet boundary condition is used for the ionic concentrations at the ends of the two reservoirs, $c_i(x = \pm 5\mu m) = C_b$. The normal ionic fluxes through all the other walls are set to be zero, $n \cdot N_i = 0$.

After solving the coupled PNP equations, the ionic concentration and potential distributions can be extracted. The resulting ionic current J_i of i^{th} species through the nanochannel can be integrated as, $J_i = \int z_i F N_i dS$, where S is a cross-sectional area of the nanochannel. The total ionic current can thus be obtained as $J = \sum_i J_i$. The averaged K^+ and Cl^- concentrations along the *x* direction is calculated by $< c_i(x) >= \int_{y=-H/2}^{y=H/2} c_i(x,y)dy / H$, where H is the channel height.

Derivations of ρ_K and ρ_{Cl}

For the un-gated area (subscript T), according to the charge neutrality condition, we can obtain,

$$[K]_T - [Cl]_T = \frac{2\sigma_s}{ehN_A} \qquad \text{(S1)}$$

According to the law of the conservation of mass, we obtain the other relationship,

$$[K]_T [Cl]_T = C_b^2 \qquad \text{(S2)}$$

Therefore, the averaged cation/anion concentrations under the un-gated area can be determined as,

$$[K]_T = -\frac{s_T}{2} + \sqrt{(\frac{s_T}{2})^2 + C_b^2} \quad \text{and} \quad [Cl]_T = \frac{s_T}{2} + \sqrt{(\frac{s_T}{2})^2 + C_b^2} \qquad \text{(S3)}$$

where $s_T = 2\sigma_s / ehN_A$ is the surface charge concentration. As a result,

$$\gamma_T \equiv \frac{[K]_T}{[Cl]_T} = \frac{(-s_T + \sqrt{s_T^2 + 4C_b^2})^2}{4C_b^2} \qquad \text{(S4)}$$

For the gated area, it is reasonable to assume that all the gate voltage is dropped on the gate dielectric. According to the charge neutrality condition, we can get,

$$[K]_C - [Cl]_C = \frac{2\sigma_s - \varepsilon_0 \varepsilon_{SiO2} V_G / d_{SiO2}}{ehN_A} \quad \text{(S5)}$$

By applying the law of the conservation of mass, we obtain,

$$[K]_C [Cl]_C = C_b^2 \quad \text{(S6)}$$

Therefore, the averaged cation/anion concentrations under the gated area can be determined as,

$$[K]_C = -\frac{s_C}{2} + \sqrt{(\frac{s_C}{2})^2 + C_b^2} \quad \text{and} \quad [Cl]_C = \frac{s_C}{2} + \sqrt{(\frac{s_C}{2})^2 + C_b^2} \quad \text{(S7)}$$

where

$$s_C = \frac{2\sigma_s - \varepsilon_0 \varepsilon_{SiO2} V_g / d_{SiO2}}{ehN_A} \quad \text{(S8)}$$

As a result,

$$\gamma_C \equiv \frac{[K]_C}{[Cl]_C} = \frac{(-s_C + \sqrt{s_C^2 + 4C_b^2})^2}{4C_b^2} \quad \text{(S9)}$$

According to the total current continuity at the micro/nano channel interfaces in the Trans side, we obtain,

$$J_T^K - J_T^{Cl} = J_{TBluk}^K - J_{TBluk}^{Cl} \quad \text{(S10)}$$

J_{TBluk}^K and J_{TBluk}^{Cl} is the K and Cl current flux in the Trans reservoir and can be assumed to have the relation of $J_{TBluk}^K = -J_{TBluk}^{Cl}$ because of an equal K and Cl concentration and a similar K and Cl mobilities in the bulk. Moreover, it is easy to see that in the nanochannel, $J_T^K / J_T^{Cl} = -[K]_T / [Cl]_T = -\gamma_T$, therefore,

$$J_T^K / J_{TBulk}^K = 2/(1+\gamma_T^{-1}) \quad \text{(S11)}$$

$$J_T^{Cl} / J_{TBulk}^{Cl} = 2/(1+\gamma_T) \quad \text{(S12)}$$

Similarly, we get the following relationship at the interface of Cis reservoir and the nanochannel ,

$$J_C^K / J_{CBulk}^K = 2/(1+\gamma_C^{-1}) \quad \text{(S13)}$$

$$J_C^{Cl} / J_{CBulk}^{Cl} = 2/(1+\gamma_C) \quad \text{(S14)}$$

It is easy to see that $J_{TBulk}^K = J_{CBulk}^K$ and $J_{TBulk}^{Cl} = J_{CBulk}^{Cl}$. Therefore, we can obtain the ratios of cation (anion) flux via the Cis side over the cation (anion) flux via the Trans side of the nanochannel as,

$$\rho_K \equiv \frac{J_C^K}{J_T^K} = \frac{1+\gamma_C^{-1}}{1+\gamma_T^{-1}} \quad \text{(S15)}$$

$$\rho_{Cl} \equiv \frac{J_C^{Cl}}{J_T^{Cl}} = \frac{1+\gamma_C}{1+\gamma_T} \quad \text{(S16)}$$

Surface charge modification

By neutralizing the intrinsic surface charge through chemical modifications, it would allow for more efficient gate modulation of the cation/anion concentration inside the nanochannel. The procedure we used in the surface charge modification is as follows.

1. Flushing the microchannel with ethanol (Sigma-Aldrich, category # 459836) for 3 hours.

2. Flushing the microchannel with 2% v/v 3-Glycidoxypropyltrimethoxysilane (GPTS) (Sigma-Aldrich, category # 440167) in ethanol (Sigma-Aldrich, category # 459836) for 3 hours.

3. Flushing the microchannel with 50 mM ethanolamine (Sigma-Aldrich, category # 411000) for 1.5 hours.

Supplementary References

43. Schwartz, G. C., Huang, Y. S. & Patrick, W. J. The Effective Dielectric-Constant of Silicon Dioxides Deposited in the Spaces between Adjacent Conductors. *J. Electrochem. Soc.* **139**, L118-L122 (1992).

44. Chandra, A. Static dielectric constant of aqueous electrolyte solutions: Is there any dynamic contribution? *J. Chem. Phys.* **113**, 903-905 (2000).